# Dynamics of highly charged ions interacting with surfaces

Bodewits, Erwin

# Chapter 5

# Total electron yields

The secondary electron yield measurements presented in this chapter are the first ones done with the IISIS setup at the ZernikeLeif facility. The measurements comprise a wide variety of ions in different charge states and different kinetic energies impinging on atomically clean Au surfaces and Au surfaces covered with thin films of $C_{60}$. In contrast to Au, $C_{60}$ is not a metal. $C_{60}$ films exhibit a band gap and therefore they are expected to behave as an insulator. Gradually changing the thin film thickness allows one to tune the surface characteristics in a controlled manner. Till now only a few pioneering experiments on hollow atom formation at thin films were done. The Oak Ridge group (Meyer et al. [14]) used Cs films on Au(011) and observed an increase in electron yield when the work function of Au was reduced by means of evaporating Cs on the surface. The Groningen group (Khemliche et al. [10] and Laulhe et al. [15]) used LiF and $C_{60}$ films on Au to study changes in the KLL Auger electron spectra of hydrogen-like C, N, and O ions when changing surface properties.

Intuitively, based on the hollow atom scenario, one could expect the number of electrons emitted due to the interaction of a highly charged ion with a surface to decrease when the surface is an insulator instead of a metal. There are three main arguments why one could expect this and which will be elaborated in the following:

The electron availability on the surface

The interaction time of an ion with a surface

The initially populated shells due to electron capture

The first argument why one would expect the electron yield to be lower for an insulator than for a metal is that the electron-hole mobility is lower in an insulator than in a metal. This would mean that after removal of some electrons from the surface, there are (almost) no electrons left at that particular spot. In a metal these holes would quickly be refilled by electrons out of the bulk material, but for an insulator this is not necessarily true, leaving the surface locally charged. In the most extreme case, this local charge up effect could lead to the bouncing back of the incoming ion before it gets fully neutralized, i.e. the so called trampoline effect [67–69]. The trampoline effect differs from 'normal' macroscopic charge up of a surface by many ions, like with the nanocapillaries (chapter 4), since the ion itself creates enough charge at the surface to be repelled.

The second argument why one could expect the number of electrons emitted to be lower in front of an insulator surface is an argument involving the time an ion spends in front of the surface. From equation 2.12 it can be seen that the distance at which the ion starts to capture electrons from a surface, is shorter for an insulator than for a metal. This would imply that there is less time available to capture and emit electrons before the ion penetrates the surface too deeply and is lost in that sense.

The third argument involves the shell into which electrons from the surface are initially captured. Since the binding energy of electrons in insulator surfaces well exceeds the work function of a metal (see fig. 2.6), the electrons which cross the potential barrier will be captured into lower shells than for a metal. This means less Auger processes are needed before the produced hollow atom is fully relaxed, which on its turn implies that less electrons will be emitted.

Experiments performed by Meissl et al. in 2008 on LiF however, showed the remarkable fact that the electron yields for LiF are actually higher than for Au [29]. The explanation given by Meissl et al. for this higher yield is that although the ion has less time to emit electrons, the escape depth for electrons is larger for LiF than for Au.

In order to investigate the neutralization and decay dynamics of highly charged ions further, thin films of $C_{60}$ were evaporated on gold. By doing so, the band gap and the work function can be slowly tuned, allowing to follow the secondary electron yield as function of the change in surface properties.

This chapter starts out with a description on how to extract from electron

statistics spectra the average number of electrons emitted in the ion-surface interaction. Section two describes the measurements which have been done on atomically clean Au to demonstrate the operational status of the IISIS setup and to illustrate general trends in electron yields. Section three describes the measurements which have been performed on monolayers of $C_{60}$.

Throughout this chapter the incidence angle $\psi$ is de ned with respect to the surface plane.

## 5.1 Data analysis

Figure 5.1 shows two typical raw electron statistics spectra for 7 keV/q $Ar^{q+}$ ions. Panel a) shows a measurement of 7 keV Ar on Au(111) under an incidence angle of 40, whereas panel b) shows 7 keV/q $Ar^{12+}$ on Au(111) with an incidence angle of 45. Although from panel b) a good estimation of the average secondary electron yield can be made, panel a) allows at most a rough estimate.

To analyze the spectra, one needs to take the following experimental facts into account: for low average yields ( g. 5.1(a)) only the probability for the emission of $n$ 1 electron(s) can be measured, where n is the number of detected electrons. The case of zero electrons emitted is not measured, but does

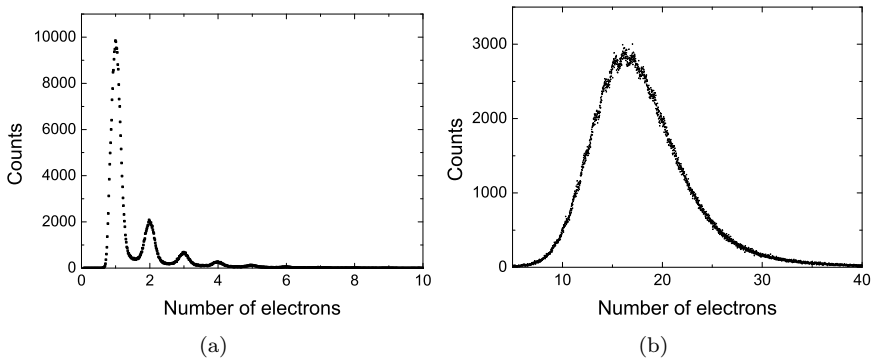


Figure 5.1: Two typical raw electron statistics spectra for ion impact on Au. For the left panel 7 keV $Ar^+$ ions impinging under an angle of 40 were used, while the spectrum in the right panel was taken with 7 keV/q $Ar^{12+}$ ions impinging under an angle of 45.

contribute to the average yield.

Another fact which has to be taken into account is the detector response to the impact of $n$ electrons, in particular the in uence of backscattered electrons on the peak shapes. For this purpose it is necessary to determine some properties of the detector and the electronics connected to it, which is described in the next section. With the detector response known, it is possible to t the spectrum and to determine the individual peak intensities. A Poisson distribution can then be tted to these values resulting in the average number of electrons emitted.

The resolution of the spectra at higher yield ( g.5.1(b)) however does not allow to t all the individual peaks. This can be remedied by tting a Gaussian distribution, as will be shown in the next sections.

### 5.1.1 Electron spectra

The shapes of the lines in the electron spectra deviate from a single Gaussian due to the backscattering of electrons at the detector surface. For a detailed description see Lakits et al. [70]. The individual peaks are centered at $nV_{det}$, where $V_{det}$ is the voltage on the detector (typically 30 kV) and n the number of electrons emitted. The full width half maximum of these peaks is experimentally determined to be around 6 keV.

When an electron backscatters, not all its energy is deposited into the detector, thereby causing the peak position to be lower than the real one. The result of this backscattering is that there is a structured \background" between the peaks. This apparent background however, is only visible for very low yields: for higher yields ($n >$10, see for example g. 5.1(b) and 5.3), the probability that one or more backscatter events occur is high, thereby fully lling up the gaps between the peaks. The electron backscattering is creating additional peaks corresponding to $m$ = 1, 2, ... $n$ backscattered electrons from the detector surface. These peaks are centered at

$$E_{nm} = (n - mk)V_{det}, \tag{5.1}$$

where $m$ is the number of backscattered electrons out of $n$ incoming electrons and $k$ is associated to the fraction of energy that the electron still has after scattering (typically $k$ is around 0.55, implying an energy deposition into the detector of 0.45 $E_0$). The full width half maximum of the backscatter peaks is given by

$$E_m = \sqrt{(E_{det})^2 + m(E)^2}, \tag{5.2}$$

where $E$ is the full width half maximum of the energy distribution of the backscattered electrons. At a detector voltage of 30 kV, the typical value for

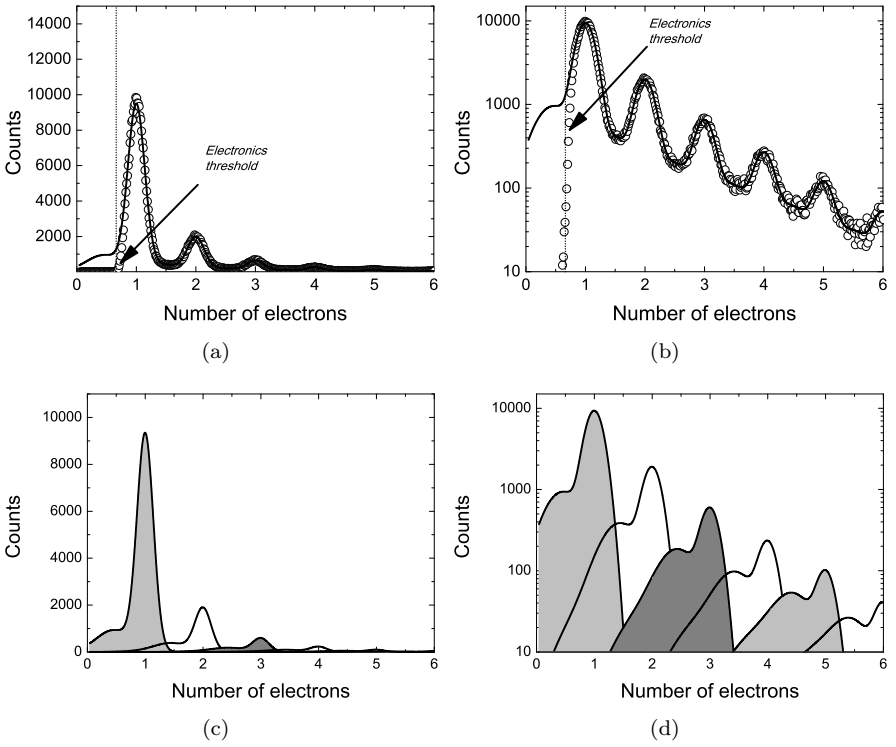


Figure 5.2: a) and b) Original raw data as in g. 5.1(a) with equation 5.7 tted to it. Also indicated is the electronics threshold. c) and d) The individual peak intensities plotted using the $C_n$ values obtained from eq. 5.7.

$E$ is 12 keV and $E_{det}$ the earlier mentioned 6 keV.
Without backscattering the full spectrum can be described by

$$S(E) = \sum_{n=0}^{\infty} C_n F_n(E), \tag{5.3}$$

where the amplitude $C_n$ is proportional to the probability of emission of $n$ electrons and $F_n$ is a Gaussian function. Taking backscattering into account,

the line shape function $F_n$ becomes

$$F_n(E) = \sum_{m=0}^{n} P_{nm} G_{nm}(E, E_{nm}, \quad E_m), \tag{5.4}$$

with $P_{nm}$ the probability of $m$ out of $n$ electrons backscattering, which is given by a binominal distribution

$$P_{nm} = \binom{n}{m} p^m (1 \quad p)^{n-m}, \tag{5.5}$$

with $p$ the single electron backscatter probability.
$G_{nm}$ is a Gaussian centered at $E_{nm}$ and a standard deviation $\sigma_m$ given by

$$\sigma_m = \frac{p}{2} \frac{E_m}{2ln2}, \tag{5.6}$$

The full spectrum is thus described by:

$$S(E) = \sum_{n=1}^{n_{max}} \sum_{m=0}^{n} C_n \binom{n}{m} p^m (1 \quad p)^{n-m} \frac{p}{2\pi} \frac{1}{\sigma_m} e^{\frac{-(E-E_{nm})^2}{2\sigma_m^2}}. \tag{5.7}$$

By tting eq. 5.7 to the data, the amplitudes $C_n$ can be determined. Figure 5.2 shows how such a t looks like in reality: panel a) and b) show the t of equation 5.7 to the data on a linear and log scale respectively, while panel c) and d) show the individual contributions of each number of electrons (n) being detected. The average yield $\gamma$ is then given by

$$\gamma = \frac{\sum_{n=1}^{\infty} nC_n}{\sum_{n=0}^{\infty} C_n}. \tag{5.8}$$

When there is an appreciable contribution to the $n$ =0 peak (no electron emission), the yield can be calculated by tting the intensities to a Poisson distribution (see section 5.1.2). Using a Poisson distribution is based on the assumption that the secondary electron emission is a statistical process.

Due to the overlap and multiplicity of the individual lines at electron yields 10, eq. 5.7 cannot be used to determine amplitudes $C_n$ reliably. In gure 5.3 it can be seen for example that for values of up to $n$ 15 individual lines can be seen, but for higher values the individual lines are no longer visible. In

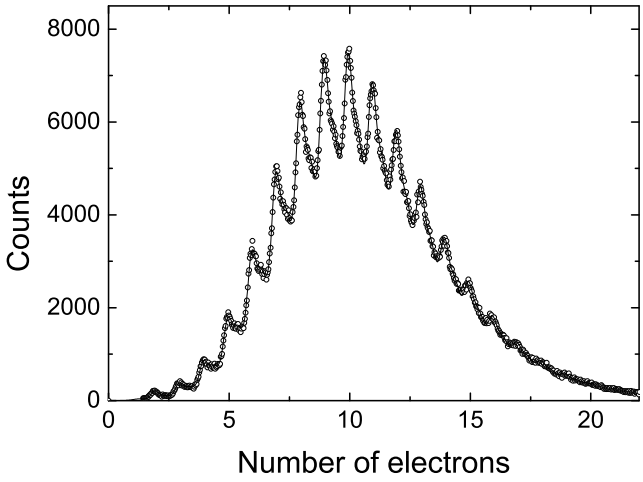


Figure 5.3: Open circles: raw data of 25 keV $Xe^{10+}$ ions impinging on $C_{60}$ under an angle of 45. Line: t according to equation 5.7. Clearly visible are the 'bumps' in between the peaks, caused by backscattered electrons.

that case a standard Gaussian distribution is tted to the data. The center of the Gaussian is related to the average electron yield $\gamma$. However due to the backscattering the center of the distribution is shifted to lower electron numbers. This shift can be accounted for by a correction factor $a_{corr}$ given by

$$a_{corr} = \frac{1}{1 \quad pk}. \tag{5.9}$$

Here, $p$ is the probability that an electron backscatters and $k$ the fraction of energy that the electron has after collision with the detector surface. Typical values for p and k are 0.16 0.02 and 0.55 0.1, resulting in a correction factor of around 1.1.

To obtain $a_{corr}$, k and p need to be known. The values for these constants can be determined by tting the spectrum at low yields to equation 5.7. Figure 5.3 shows how well such a t looks like. The presence of the backscattered electrons can be clearly seen. In the experiments presented in this thesis the correction factor is determined for every run. This can be achieved by either using an ion with a relative low charge state, or by using a 'contaminated beam'.

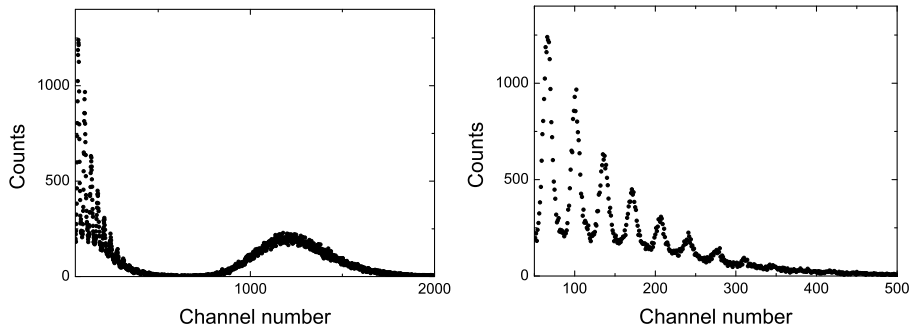


Figure 5.4: a) Full spectrum from 7 keV/q $^{131}Xe^{22+}$ and $^{12}C^{2+}$. b) Enhancement of the spectral part containing the $C^{2+}$ beam.

In case of a'contaminated beam', a second ion beam species with (nearly) the same mass-over-charge ratio is also entering the chamber, because the 110° (analyzing power of 0.5%) magnet in the beamline cannot separate these two beam components (completely) from each other. An example of such a situation is shown in gure 5.4, where panel a) shows the full spectrum showing $^{131}Xe^{22+}$ and $^{12}C^{2+}$ and panel b) is an enhancement of the left part i.e. the undesired carbon beam which can be used bene cially to determine the correction factor $a_{corr}$.

Apart from the correction factor, the calibration of the x-axis is also deduced from the tting procedure: the separation between the individual peaks tells how many channels correspond to the energy deposited by a single electron. If no changes are made to the electronics, this number of channels should always be the same. In order to determine where the zero of the x-axis is located, a few measurements with di erent detector voltages have to be done. These measurements give the number of channels per detected electron for each given voltage, thereby allowing to determine the crossing of these lines and thus the zero value of the axis.

### 5.1.2 Electron number distributions

Following the common assumption that secondary electron emission is a purely statistical process implies that the electron number distribution can be described by a Poisson distribution. Because deviations from a Poisson have been found,

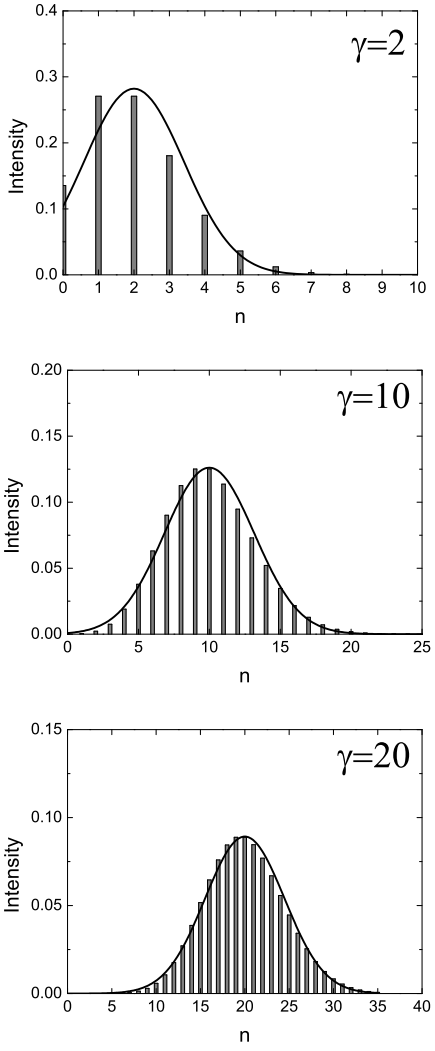


Figure 5.5: Comparison of Poisson (bars) and Gauss (curves) distributions for di erent values of $\gamma$.

several other distributions were suggested [51, 70{73]. None of these distributions was found to be generally applicable. Therefore, when necessary, a Poisson distribution will be used to determine the probability of zero-electron emission.

For low yields ($\gamma$ 10) the procedure described in the previous section is used to obtain the individual peak intensities $C_n$ which are then tted to a Poisson distribution. The Poisson distribution is given by

$$P_n(\gamma) = \frac{\gamma^n}{n!} e^{-\gamma}, \tag{5.10}$$

where $\gamma$ is the average yield. For the Poisson distribution it can be derived [74] that the standard deviation is given by the square root of the average, which in this case means $\sqrt{\gamma}$. For high values of $\gamma$ eq. 5.10 converges to a Gaussian distribution given by

$$G(n, \sigma, \gamma) = \frac{1}{\sqrt{2\pi}\sigma} e^{-\frac{(n-\gamma)^2}{2\sigma^2}}, \tag{5.11}$$

where $\sigma$ is the standard deviation and in this very particular case, i.e. in the limit $\gamma$ 1, $\sigma$ is equal to $\sqrt{\gamma}$ thus resulting in

$$G(n, \gamma) = \frac{1}{\sqrt{2\pi\gamma}} e^{-\frac{(n-\gamma)^2}{2\gamma}}. \tag{5.12}$$

This implies that the average electron yield $\gamma$ can be determined both from the central peak position as well as the width of the distribution.

Figure 5.5 shows the comparison for various values of $\gamma$, of a Gaussian distribution and a Poisson distribution. It can be clearly seen from the gure that the Gaussian distribution is symmetric, whereas the Poisson distribution has an asymmetric shape with a long tail. For $\gamma$ equal to 2 the agreement is rather poor, while for $\gamma$ equal to 20 both distributions are basically identical. Therefore for low values of $\gamma$, say $\gamma$ 10, a Poisson distribution should be used while for higher values of $\gamma$ a Gaussian distribution can be safely and conveniently used.

As practical illustration, gure 5.1(a) is further analyzed here. First the data is tted to eq. 5.7, which gives the backscatter probability p to be 0.18 and k to be 0.55. Also the values of $C_n$ (the individual peak intensities) are found by tting the spectrum to this equation. Figure 5.2 (c) and (d) show what the individual contributions look like on a linear scale and a log scale, using the $C_n$ values obtained by this tting procedure, panels (a) and (b) show the ts to the data.

The intensity of the individual peaks are then tted to a Poisson distribution and for illustrative purpose to a Gauss distribution as well. The results are

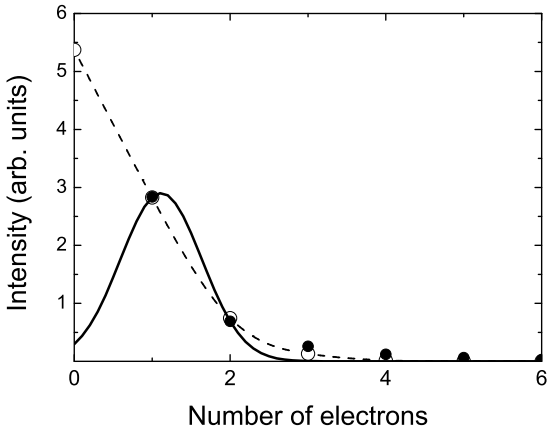


Figure 5.6: The extracted intensities of the number of electrons emitted in 7 keV $Ar^+$ impinging on Au at an angle of 40° $C_n$ (black closed circles, data from g. 5.1) with a Poisson distribution with $\gamma$ = 0.53 (open circles connected by dashed line) and a Gauss distribution with $\gamma$ = 1.12 (solid line) tted to them.

depicted in gure 5.6. It can be clearly seen that the Poisson function represents the better t: the tail of the distribution is totally missing in the case of a Gaussian distribution. In addition, and in this case most importantly, the large di erence of one order of magnitude between the Poisson and Gauss distribution for $n$ = 0 is of note, which results in a factor of 2 di erence in the average yield. In numbers, the Poisson distribution yields $\gamma$=0.53 while assuming a Gaussian distribution yields $\gamma$=1.12.

In order to check in more detail whether a distribution is indeed behaving like a Poisson distribution, the simple relation

$$\gamma = (n + 1) \frac{C_{n+1}}{C_n} \tag{5.13}$$

needs to be full lled (cf. eq. 5.10). The outcome of such a check on the results of g. 5.1 is shown in g. 5.7. If the data would ful ll this condition, the points would lie on the indicated dotted line of $\gamma$ = 0.53. The fact they are not lying on this line shows that, in this example, for the higher electron numbers the Poisson distribution is underestimating the larger electron numbers in the data. This hints at a second (weak) class of interactions, having a di erent somewhat higher electron yield [75].

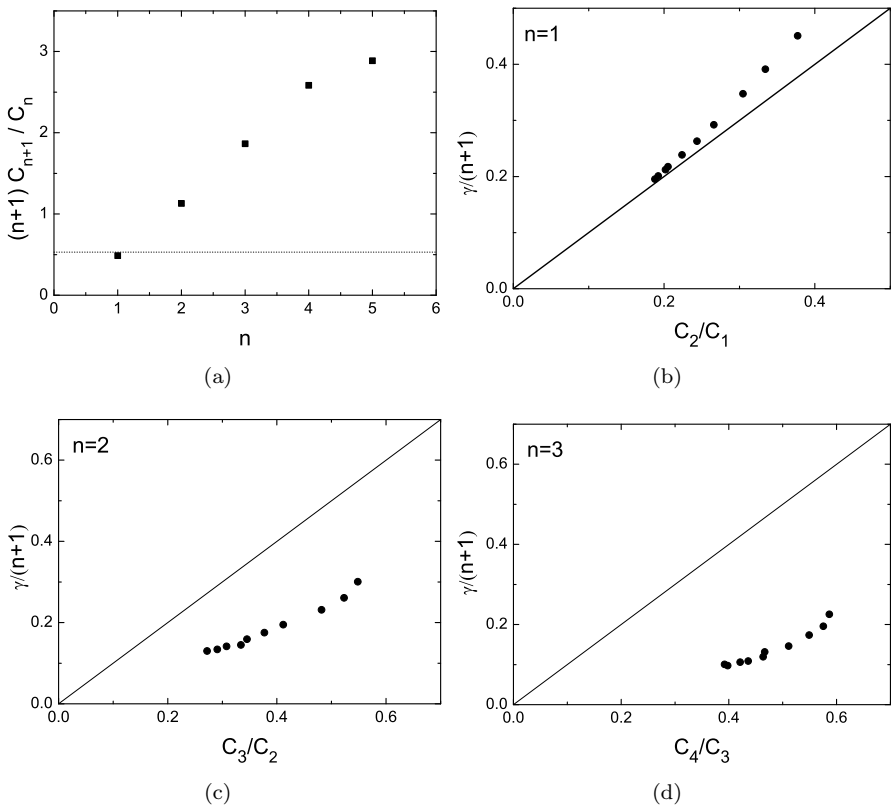


Figure 5.7: a) The values of $C_n$ from one spectrum (dots) and the obtained yield of $\gamma$=0.53 (dashed line). Panel b, c, and d show the ratio of $C_{n+1}/C_n$ vs $\gamma/(n+1)$ for different values of $n$, obtained from multiple spectra.

The same procedure has been repeated for a series of spectra taken with 7 keV $Ar^+$ under different incidence angles. For all these spectra the $C_n$ values have been determined. Figure 5.7 shows $\gamma/(n+1)$ as a function of $C_{n+1}/C_n$. Here, it is obvious that for $n$ = 1 (panel b) the results agree rather well, whereas for higher $n$ values, and thus the tail of the distribution, the spectra deviate from a pure Poisson distribution. A similar behaviour has been observed by Lakits et al. [70]. There, H, He, Ne and Ar ions with a kinetic energy ranging from 1-16 keV have been used. The fact that for higher $n$ values the data fall below

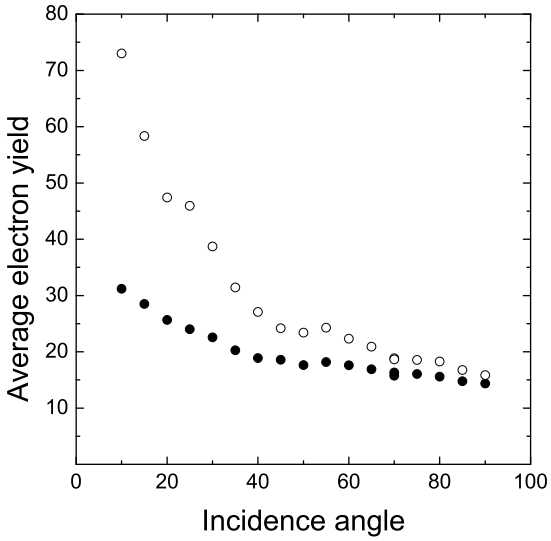


Figure 5.8: The average secondary electron yield of 91 keV $Ar^{13+}$ ions on Au(100) as function of incidence angle. The yields were determined either on basis of the peak position (closed circles) or the width (open circles) of the Gauss tted to the secondary electron spectrum.

the $\gamma/(n+1)$ curve hints again at a contribution with a higher average electron yield. These e ects will be discussed in more detail in section 5.2.

In order to analyze a spectrum with a higher yield, i.e. g. 5.1(b), a Gauss function is tted to the raw data. As described earlier, the average electron yield is then found from the centroid of the Gauss by applying a small ( 10%) correction factor (eq. 5.9) to the position of the centroid. Since the Gaussian function is expected to be a limit of a Poisson distribution, the squared standard deviation of this Gaussian should yield the same $\gamma$ value. In order to investigate this further, an angular scan has been performed with $Ar^{13+}$ ions on Au(111). The average electron yields determined from the center and the width of the spectrum are plotted in gure 5.8. As can be seen, for tilt angles of 40 degree and above the relation $\gamma = \sigma^2$ yields slightly higher $\gamma$ values than the peak positions suggest. For tilt angles below 40 degree, the two sets of $\gamma$ results start to diverge more and more as the tilt angle decreases.

In order to see whether the tting itself can be improved, the data taken

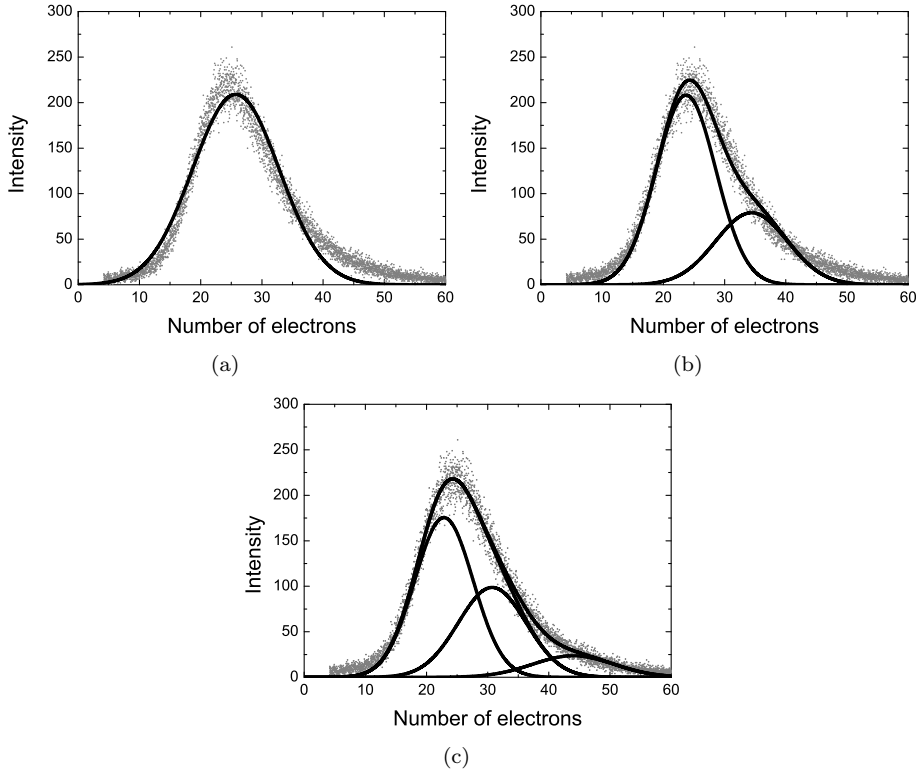


Figure 5.9: 91 keV $Ar^{13+}$ impinging under an angle of 15° on Au(100). Panel a) shows how the fit looks like with one Gaussian function fitted to the data, while in b) and c) more Gaussian functions are added.

at an incidence angle of 15° are shown in fig. 5.9 with one, two and three Gaussian functions fitted to it. Here it has to be noted that in the fit with a single Gaussian function the standard deviation is taken as a free parameter, whereas both for the fit with two and three Gaussian functions the standard deviation is set to $\sqrt{\gamma}$.

For one Gaussian function it is obvious that the lower and higher electron numbers are not properly represented by the Gaussian distribution, resulting in a too broad distribution. Of course, this improves when more Gaussian functions are added. The additional contributions may be linked to different trajectory

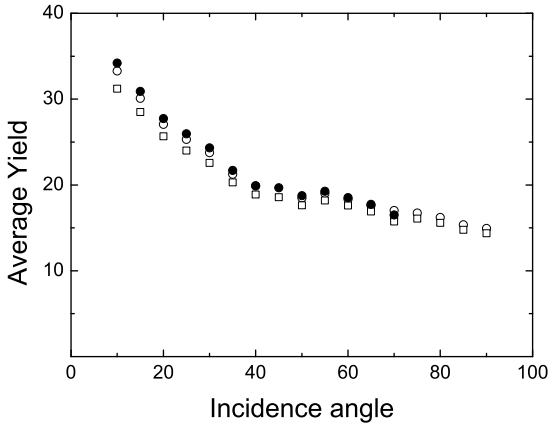


Figure 5.10: The electron yields of 91 keV $Ar^{13+}$ ions on Au(100) as function of incidence angle, with 1 (open squares), 2 (open circles) and 3 (closed circles) Gauss distributions fitted to it.

classes. This will be described in more detail in section 5.2.

When the weighted average of the Gauss distributions is taken however, the average electron yield $\gamma$ is only a bit higher ( 15%) than the value deduced from the single-Gaussian function fit. Also, for larger incidence angles, one Gaussian function seems to be sufficient to find the average electron yield. Figure 5.10 shows a compilation of the average electron yields for 91 keV $Ar^{13+}$ impinging on Au(100) determined by using one, two, or three Gaussian functions to represent the spectra. Clearly visible is that for low incidence angles the average electron yield starts to differ slightly, but for the somewhat higher angles they become almost the same. Therefore, normally the spectra analyzed in this thesis are fitted to a single Gaussian function.

Finally, in order to obtain an impression of how well reproducible the electron number statistics measurements are, the electron yield of 91 keV $Ar^{13+}$ as a function of incidence angle has been measured several times, on different days with weeks between the first and last measurement. Figure 5.11 compares the results of these measurements. First of all, one notices the very good agreement between the data sets, demonstrating the reproducibility. Another noticeable fact is that the results obtained on a single day all seem to deviate the same way from the average. In figure 5.11 for example it can be seen that all closed circles are below the average, whereas the closed triangles are all above the average.

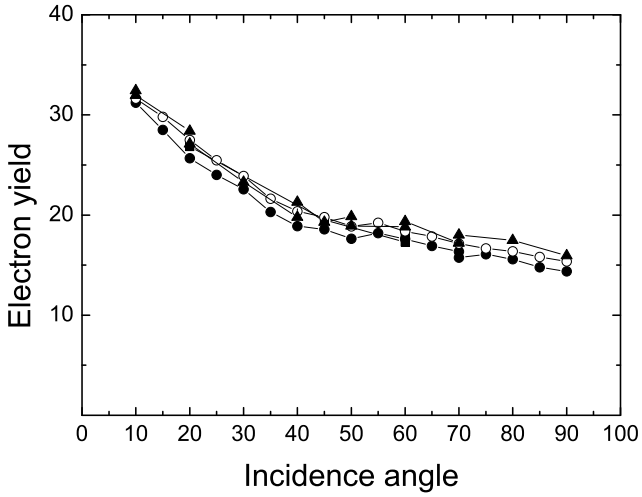


Figure 5.11: The electron yield of 91 keV $Ar^{13+}$ ions on Au(100) as function of incidence angle, measured on several di erent days.

This suggests that the small di erences between data sets are not purely statistical but also have a systematic component. To illustrate this more clearly, gure 5.12 shows the data relative to the average of all 4 di erent measurements for every incidence angle taken, and the average. It becomes clear that the di erences between the measurements done at di erent days are small: the standard deviation obtained from the normalized data is 0.036. In the following we will assume conservatively an uncertainty associated with the electron yield measurements of 5%.

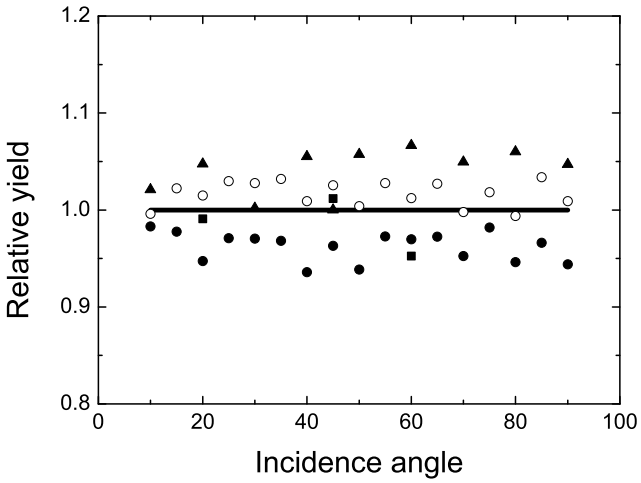


Figure 5.12: The electron yield of 91 keV $Ar^{13+}$ ions on Au(100) as function of incidence angle, relative to the average of all data for a speci c incidence angle.

## 5.2 Electron emission from hollow atoms at Au surfaces

In this section we will discuss aspects of the electron yields of slow highly charged Ar and Xe ions interacting with clean Au. Of prime interest is the electron emission resulting from the transient hollow atom, i.e. the electron emission driven by the potential energy carried by the incoming HCI. In the hollow atom scenario (see chapter 1) the HCIs get resonantly neutralized into highly-excited states that decay by Auger processes generating mainly low energy electrons of 5-15 eV [76{79]. In the most simpli ed approach all the potential energy is converted into low-energy Auger electrons and the yield becomes directly proportional to the potential energy. For ions in charge states of 3+ to 8+ Arifov et al. [80] found a proportionality factor on the order of 1/50. By further increasing the charge state the potential energy can be dramatically increased. For xenon, for example, a 28+ ion already has a potential energy of 12 keV. On basis of the above approach, one might then expect hundreds of electrons.

For a whole variety of such very highly charged ions Aumayr and coworkers [29, 70, 81{84] have performed pioneering experiments on the dependence of secondary electron yields on the charge state and species of the projectile ions. In order to look into this for intermediate charged HCI's (10-25+) and as a rst test of the newly developed IISIS setup, we used 70 keV Ar (7+ to 13+) and Xe (10+ to 26+) ions. The ions were scattered on Au(100) at an incidence angle of 45°. Fig. 5.13 shows how the electron yield increases strongly when higher charge states are used. From this gure, one sees that on average the yields for Ar ions are higher than the ones obtained for Xe ions in the same charge state. Furthermore the data are in very good agreement with comparable measurements done by Aumayr and coworkers [83, 84] (not shown here) indicating that our new IISIS set up is operating to speci cations i.e. reproduces established results.

In gure 5.14 the same data are shown but now as function of the potential energy of the HCIs. The numerical values of the total potential energy, taken as the sum of all ionization potentials up to the speci ed charge states for Ar and Xe, are tabulated in Appendix B. In gure 5.14 it can be seen that the di erence between the electron yields from Ar and Xe ions impinging on Au disappears by and large when plotting the data as function of the potential energy instead of charge state.

In addition, in this regime the increase in electron yield is approximately linear to the potential energy of the ion. However, the proportionality factor

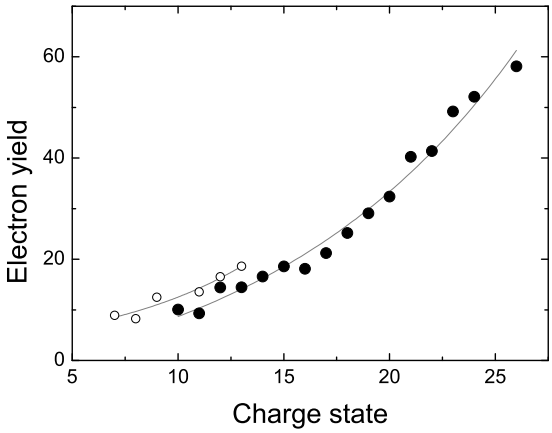


Figure 5.13: The electron yield as a function of charge state of the ion for Xe (closed circles) and Ar (open circles) with a kinetic energy of 70 keV. The thin lines are merely to guide the eye.

is around 1/150, which is thrice as small as the one at lower charge states [80]. Kurz et al. [81, 83] have shown that for even higher charged ions the factor reduces even further, in particular when initially K and L shell core vacancies are present ($q > 44+$ for Xe and $q > 8$ for Ar). Filling of the inner shells by Auger processes will lead to energetic electrons, which would be so energetic that only a small part of them will be attracted towards the detector. Moreover, these fast Auger electrons carry away a larger part of the potential energy, which is then not available for emission of slower electrons. However, for heavier elements relaxation by X-ray emission becomes rapidly more important than Auger transitions and will dominate the lling of the K-shells. Moreover the lling of the inner shells may not be fast enough and full relaxation of the ion might not be reached before it penetrates the surface. The last part of the hollow-atom dynamics takes then place below the surface and not all the electrons that are emitted will escape into the vacuum. Taking all these e ects into account, this leads to a reduction in the number of electrons emitted. On the other hand extra electrons may originate from the peeling o [37, 85, 86] of electrons from the hollow atom up on entering into the electron selvedge of the surface or from scattering of energetic innershell Auger electrons in the target which may lead to additional secondary electrons.

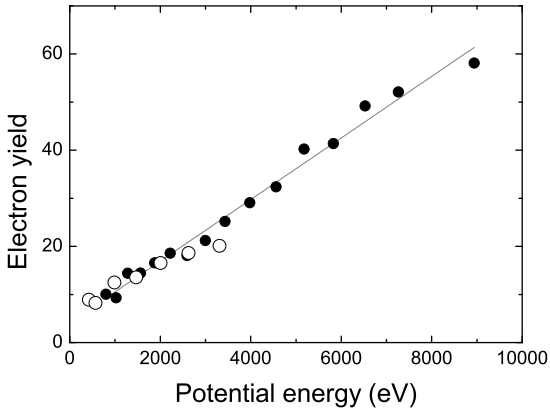


Figure 5.14: The electron yield as a function of potential energy carried by the ion for Xe (closed circles) and Ar (open circles) with a kinetic energy of 70 keV. The thin line is merely to guide the eye.

Following Eder et al. [87] the electron yield $\gamma$ can be divided in two main components, one arising from the projectiles potential energy ($\gamma_p$) and one from its kinetic energy ($\gamma_k$). One can distinguish three contributions to the potential emission $\gamma_p$:

> Low-energy electrons from the autoionization relaxation of the hollow atom supported by fast electronic transition transitions between the projectile and the surface '$\gamma_{pa}$'.
>
> Low-energy electrons from the promotional peeling o of electrons by the enhanced electronic screening upon entering the target selvedge '$\gamma_{pp}$'.
>
> Energetic electrons from lling of inner shells which occurs mainly below the surface and low-energy secondary electrons produced by these energetic electrons in the target '$\gamma_{pi}$'.

For the kinetic emission one can identify two main processes:

> Collisions of the projectile with the target electrons '$\gamma_{kc}$'.
>
> Electron promotion into the continuum in projectile collisions with individual target atoms '$\gamma_{kp}$'.

The total electron yields $\gamma$ measured in the experiments are thus equal to:

$$\gamma = \gamma_p + \gamma_k = \gamma_{pa} + \gamma_{pp} + \gamma_{pi} + \gamma_{kc} + \gamma_{kp}. \quad (5.14)$$

Information on the hollow-atom dynamics is contained in $\gamma_p$ and in particular $\gamma_{pa}$. This should be best accessible at low kinetic energies because below a certain velocity threshold, kinetic electron emission due to direct projectile electron collisions [87] is inhibited. The threshold velocity of the projectile $v_{th}$ is given by:

$$v_{th} = \frac{1}{2} v_F \left(\sqrt{1 + \frac{W_\phi}{E_F}} \quad 1\right), \quad (5.15)$$

where $v_F$ and $E_F$ are the Fermi velocity and energy respectively.

For the Au targets used in this research, the threshold velocity is approximately 2.8 x $10^5$ m/s which corresponds to an energy of 400 eV/amu. Most of our experiments have been performed below or somewhat above $v_{th}$. The most energetic Ar and Xe ions used are 91 keV $Ar^{13+}$ (2.3 keV/amu) and 182 keV $Xe^{26+}$ (1.4 keV/amu). On basis of the results of Eder et al. for $Ar^+$ and $Xe^+$ one can estimate a kinetic energy driven yield $\gamma_k$ (note $\gamma_k = \gamma_{kc} + \gamma_{kp}$) of roughly 3 electrons per incoming 91 keV $Ar^{13+}$ or 182 keV $Xe^{26+}$ ion under an incidence angle of 90 and which is a function of $1/v_\perp$ [88].

This reduces $\gamma$ to $\gamma_p + \gamma_{kc}$ of which $\gamma_{pa}$ is most directly linked to the hollow-atom electron dynamics. Previous experiments [29, 81, 89] have given evidence for an empirical relation between the yield and the normal velocity in which $\gamma_{pa}$ is inversely proportional to the square root of the velocity component normal to the surface and thus the square root of the interaction time. $\gamma_{pp}$ depends only weakly on the velocity [37, 81] and remains virtually constant in the energy regime where the present experiments are performed. $\gamma_{pi}$ is most relevant for very highly charged ions carrying deep-lying K and L shell vacancies. Here intermediately charged Ar and Xe ions are used. All this suggests the following simple relation for the electron yields as function of normal velocity $v_\perp$:

$$\gamma = \gamma_\infty + \frac{c}{\sqrt{v_\perp / v_0}} + \frac{\gamma_{kin}^{\psi=90}}{v_\perp / v_0}. \quad (5.16)$$

Here, $\gamma_{kin}^{\psi=90}$ is taken from Eder et al. [87] and is taken as zero for energies below the kinetic threshold. The simplest way to change $v_\perp$ is done by changing the incidence angle while keeping the total kinetic energy and therefore velocity constant, since $v_\perp = v_0 \sin\psi$. This has been done for 91 keV $Ar^{13+}$ ions impinging on Au(100), from 10° up to an incidence angle of 90 and is shown in

g. 5.15. When plotted as function of the incidence angle, the data should be proportional to $\sin(\psi)^{-0.5} + \sin(\psi)^{-1}$

If the yield is indeed proportional to this factor, it would mean that for higher incidence angles ($\psi$ 70°) the yield should barely change. This has been con rmed by other groups [29, 90, 91]. However, gure 5.15 shows that for $\psi$ 70° the electron yield continues to decrease. The reason for this lies in the geometry of the experimental setup. The secondary electrons which are emitted due to ion-surface interaction are typically emitted into all directions and when near{normal incidence angles are used, many electrons are emitted away from the detector. Although most of them are still detected, it is unavoidable that some of them will not make it towards the detector. At normal incidence angle the fraction of not detected electrons is estimated to be 10{20%, depending on the energy of the electrons. In principle this could be corrected for by simulating the collection e ciency and correct the measured electron yield afterwards [90]. In order not to introduce any additional uncertainty, this is not done but instead only the data up to an angle of 60° are used for further data analysis.

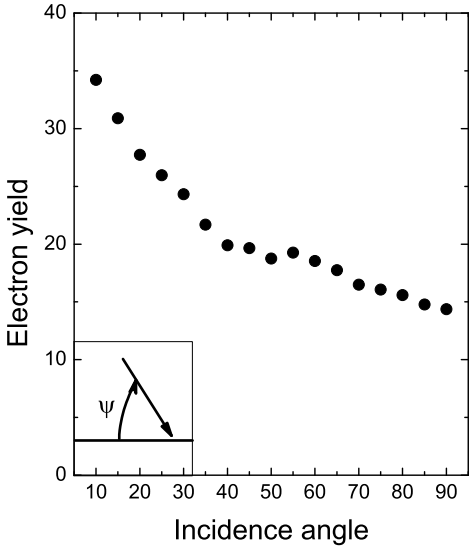


Figure 5.15: The electron yield as a function of incidence angle $\psi$, for 91 keV $Ar^{13+}$ ions impinging on Au(100).

In order to see whether the data up to 60° obey equation 5.16, the incidence angle has been transformed to the perpendicular velocity towards the surface. The results are shown in figure 5.16. Here it can be seen that a fit according to equation 5.16 fits the data very well.

To check whether the perpendicular velocity towards the surface is the only parameter determining $\gamma_\infty$, a series of measurements has been conducted with different initial kinetic energies $E_0$. Also, for every given initial kinetic energy, an angular scan has been made. Figure 5.17 compiles the results of these measurements. The initial kinetic energies $E_0$ used are 4, 12, 40, 80 and 91 keV respectively, resulting in perpendicular velocities towards the surface in the range of $3.6 \cdot 10^4$ to $6.2 \cdot 10^5$ m/s. The lines shown in figure 5.17 are fits according to equation 5.16, where a single value for $\gamma_\infty$ is used for each individual fit. Clearly it can be seen that they describe the data well. From the top right down to the bottom left the initial kinetic energy goes down: the closed circles are points belonging to 91 keV, whereas the closed triangles belong to the 4

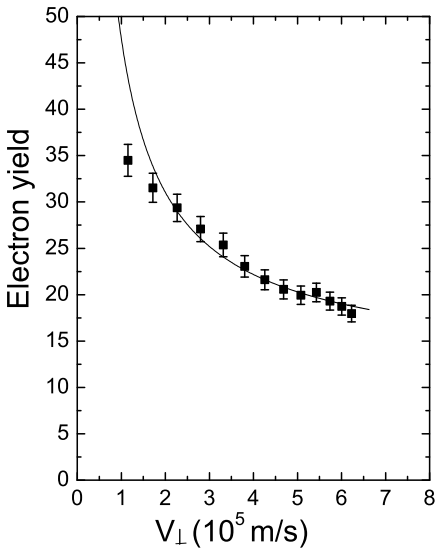


Figure 5.16: The electron yield as function of perpendicular velocity. The line is a fit using equation 5.16 and ends at the velocity which corresponds to 90° incidence angle.

keV series. It can be seen that for the same $v_\perp$ the electron yield increases with total kinetic energy. Using 91 keV $Ar^{13+}$ the maximum electron yield is as high as nearly 35 electrons, while using 4 keV $Ar^{13+}$ with the same normal velocity the yield is only halve of this i.e. 17. Having obtained the $t$ parameters, it is now possible to separate the potential and kinetic contributions to the secondary electron yield. As visible in g. 5.18, the contribution due to the potential energy (black closed dots) of the ion is lying on a single curve, whereas the contribution due to the kinetic energy (gray closed circles) of the ion varies with the initial velocity of the ions.

The magnitude and direction of the initial velocity has a major in uence on

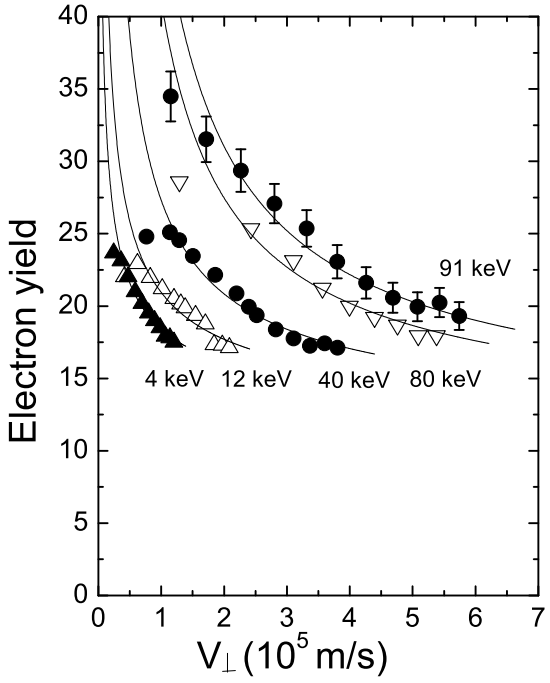


Figure 5.17: The electron yield as function of di erent perpendicular velocities towards the surface using $Ar^{13+}$ ions with di erent initial kinetic energies (see text) and di erent incidence angles. The lines are $t$s according to equation 5.16 and end at velocities which correspond to 90° incidence angle.

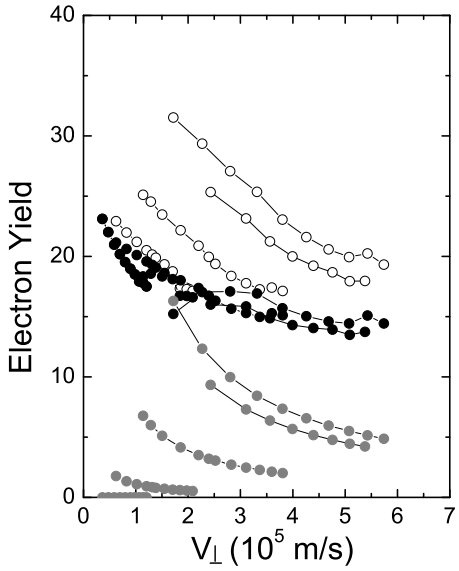


Figure 5.18: The potential electron-emission yields for $Ar^{13+}$ ions colliding on Au(100) as function of the perpendicular velocity (black closed symbols). The yields are determined by subtracting the kinetic contribution (grey symbols) from the total yields (open circles).

the trajectories of the ions. Figure 5.19 depicts very schematically three classes of trajectories:

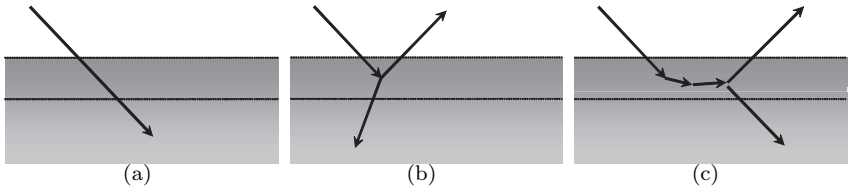


Figure 5.19: Tentative scenario of di erent trajectories: a) Ions penetrating the surface 2) Binary collisions c) Scattering along/below the surface.

1. penetration of ions into the bulk before a rst hard atomic collision takes place.

2. the rst hard collision takes place near the surface after which the ions are backscattered out of the crystal or penetrate deeper into the sample.

3. as 2) but the ions get scattered in a near-surface plane leading to long near surface trajectories.

The di erent classes of trajectories may have di erent electron yields.

By means of coincidence measurements of scattered particles and electron yields for 18 keV $Ar^{8+}$ ions impinging on Au(111) under grazing incidence angle Lemell et al. observed di erent trajectories which have an electron yield of 7 and 15 electrons respectively [75, 91].

For the experiments shown in g 5.16 the initial velocity of the ions was kept xed and the velocity perpendicular to the surface changed by changing the angle of incidence. At large, near-normal incidence most of the 91 keV Ar projectiles will penetrate into the target and only a small fraction will scatter o the surface. When lowering the incidence angle more projectiles will scatter o the surface and the number of sub-surface trajectories will get reduced. At even smaller angles of incidence, long above surface trajectories become feasible. Since interaction times and trajectory lengths di er for the three classes of trajectories, the electron yields for each class of trajectories di er. Therefore, one can expect that when going from normal to grazing incidence impact of 91 keV $Ar^{13+}$, contributions of subsurface trajectories will decrease, while the role of binary surface trajectories and later on also above surface trajectories will increase.

For $Ar^{13+}$ it is already shown in gure 5.9 that multiple Gauss distributions t the data better then a single Gauss distribution. When each of these Gauss distributions is associated with a di erent class of trajectories, the broadening of the spectra at low incidence angles can be understood. In order to be able to investigate this further, each individual spectrum measured during the angular scan with 91 keV $Ar^{13+}$ shown in gure 5.15 has been tted with 3 Gauss functions. Figure 5.20 shows the contributions of each of the individual Gauss distributions to the total t for all incidence angles. Clearly it can be seen that for larger incidence angles only two contributions can be identi ed. For smaller incidence angles however, a third component appears.

At near normal incidence energetic 90 keV Ar projectiles will deeply penetrate the target, there it is likely that the strongest component at large incidence angles (closed circles in gure 5.20) are linked to penetrating trajectories. Then

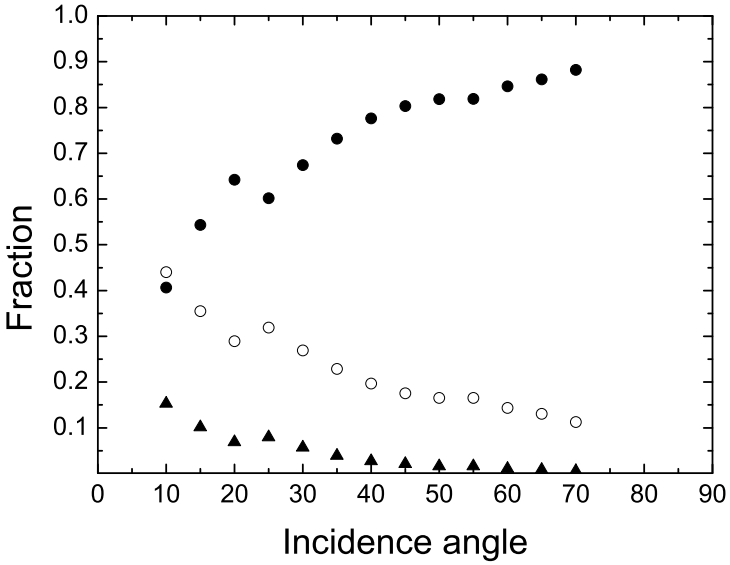


Figure 5.20: The individual contributions of the 3 Gauss functions tted to the spectra for 91 keV $Ar^{13+}$ with di erent incidence angles (for an example, see g. 5.9). The di erent contributions may be identi ed as penetrating (closed circles), binary collisions (open circles) and long near the surface trajectories (closed triangles).

the other contribution (open circles) should be linked to binary scattering o the surface. This is in line with the trend that when lowering the angle of incidence penetrating trajectories become less. At even smaller angles a third component (closed triangles) appears which should then be due to long \surface" trajectories for which one expects the highest electron yields. Indeed, the third component shows up at the highest electron numbers (cf. gure 5.10). Note that at real grazing angles of incidence (theta 10°) grazing above surface trajectories become of importance which are expected to yield lower electron yields [75].

When tting the spectra taken with 4 keV Ar $^{13+}$ ions however, it becomes clear that multiple trajectories play a much smaller role compared to the 91 keV $Ar^{13+}$ series. When looking at the intensity of the two Gauss functions, see gure 5.21, one sees that even for the lowest incidence angle of 15° the contribution

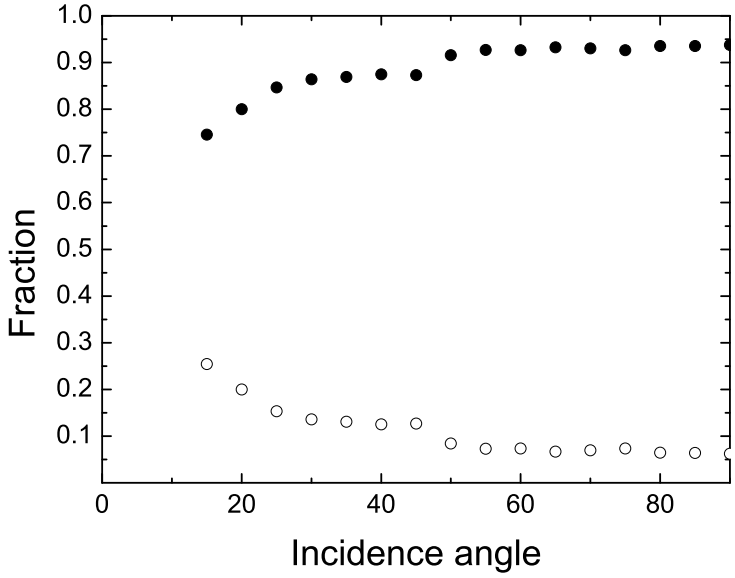


Figure 5.21: The individual contributions of the 2 Gauss functions tted to the spectra for 4 keV $Ar^{13+}$ with di erent incidence angles.

is around 25% whereas in the case of 91 Å$^{13+}$ the second and third Gauss contribute to around 60% of the total spectrum. These observations are in line with the idea of di erent trajectory classes that contribute to the total electron yield observed.

To check the validity of this scenario simulations have been performed with SRIM [92]. Although SRIM does not simulate the neutralization and relaxation of the HCI at the surface, it allows to get an idea about the trajectories the ions undergo. As separation between penetrating (class 1) and near-surface trajectories (class 2) the second atomic layer of the Au crystal was taken. Class 3 of long near-surface trajectories was de ned of having at least 3 collisions above the second atomic layer. Figure 5.22 shows the result of the simulations, and the normalized amplitudes of the three di erent Gauss distributions intensities for di erent incidence angles. Here, the Gauss distribution intensity labeled 1 is connected to the lowest yield and thus penetration in the surface. Number 2 is connected to the center Gauss line (cf. g. 5.9c) and connected to the trajectories representing a single binary collision above the second atomic layer.

The last one, number 3, is the class of trajectories associated with trajectories along the surface. First of all, it should be noted that all three processes change gradually in both the experiment and the simulations. Further clarifying these e ects requires more experiments to be done, supported by trajectory calculations.

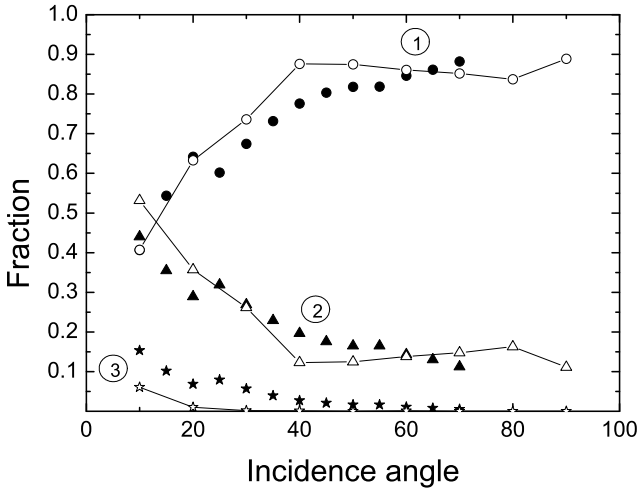


Figure 5.22: Normalized fractions of the three components contributing to the electron number spectra in comparison to the SRIM intensities for the three di erent trajectory classes, see text.

## 5.3 Hollow atom dynamics on thin films of $C_{60}$ on Au

This section will describe the first work done on total electron yields of HCI interacting with thin films. So far, the only work done with highly charged ions interacting with thin films focused on the change in the KLL Auger electron spectra as function of surface coverage i.e. workfunction change [10, 14, 15].

In order to study the total secondary electron yield on thin films, monolayers of $C_{60}$ have been evaporated on Au. By evaporating monolayers of $C_{60}$ on the surface, a band gap in the surface density of states (SDOS) is introduced [93]. This band gap makes the surface behave like an insulator instead of a metal.

The evaporation of $C_{60}$ layer by layer allows to measure the electron yield as function of layer thickness and to investigate the transition from a metal towards an insulator. When there is only one monolayer, one would intuitively expect that when the ions penetrate the surface, they will soon encounter the Au bulk material below the first monolayer of $C_{60}$.

Figure 5.23 shows how the electron yield is affected by the thin film thickness for a wide range of projectile charge states. More specifically, 70 keV $Xe^{q+}$ ions with $q$ ranging from 10 to 26 are used impinging under an angle of 45°. As before, when the charge state of the ion is increased, an increase in secondary

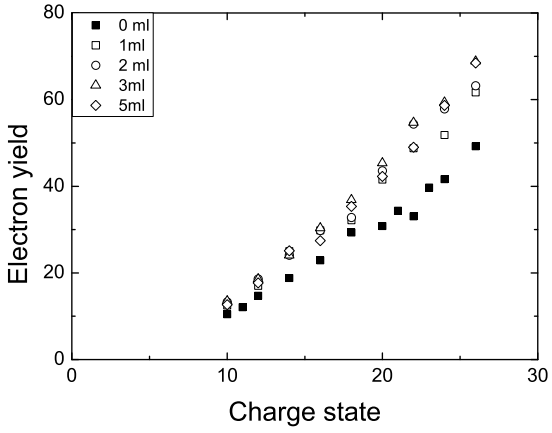


Figure 5.23: The electron yield as function of charge state for different thin film thicknesses of $C_{60}$ evaporated on Au(111).

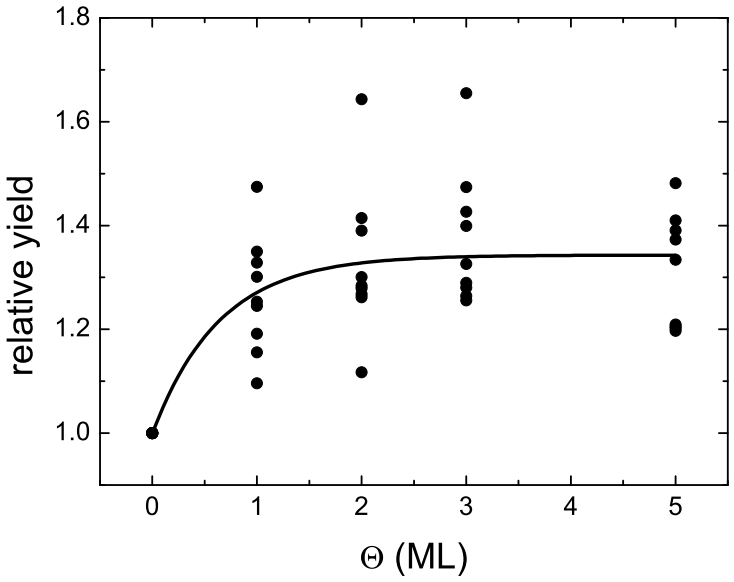


Figure 5.24: The electron yield as function of charge state using 70 keV $Xe^{q+}$ for different thin films thicknesses of $C_{60}$ evaporated on Au(111).

electron yield $\gamma$ is observed for all layer thicknesses of $C_{60}$ used. Furthermore a clear increase in electron yield as function of layer thickness is seen: for 0 monolayers (clean Au(111)) the electron yield is around 50 electrons for $q$=26, while the yield is as high as nearly 70 electrons for 3 and 5 monolayers of $C_{60}$ deposited, meaning an increase of around 40% compared to clean gold.

In order to study the evolution of the secondary electron yield $\gamma$ as function of layer thickness, figure 5.24 shows the relative increase in secondary electron yield per monolayer evaporated. Here, every different charge state has been divided by the electron yield obtained at clean Au with the same ion.

The remarkable fact that the largest change in electron yield already occurs after evaporation of a single monolayer is clearly visible from the figure. All the data points together (from $q$=10 to $q$=26) have been fitted to an exponential depending on layer thickness. This curve is shown together with the data points (see figure 5.24). From this fit it can be seen that after deposition of 2 to 3 monolayers of $C_{60}$ there is no noticeable change anymore of the electron yield. This implies that within 2–3 ML the same electron yields are established as on

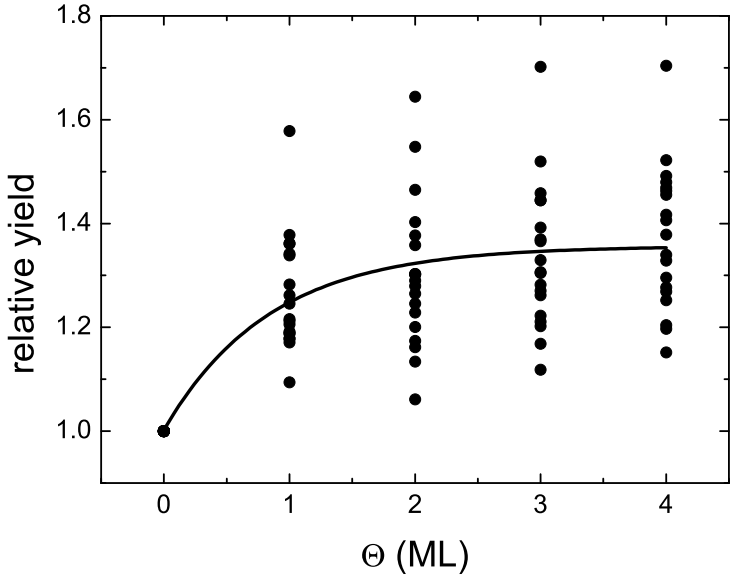


Figure 5.25: The electron yield as function of charge state using 70 keV Xe for different thin film thicknesses of $C_{60}$ evaporated on Au(100)

bulk $C_{60}$ (thick layers).

The same measurements have been performed on an Au(100) surface. The electron yields obtained using this surface are depicted in figure 5.25. Here, the same trend is again visible: when the number of monolayers of $C_{60}$ is increased, the electron yield is increasing as well. Similar to the Au(111) surface, changes in electron yield above 2 or 3 monolayers are rather small according to the fit.

In order to compare the electron yield from both surfaces, the electron yield as function of charge state of the ion is shown in figure 5.26. Here, every panel shows the electron yield for a different number of layers of evaporated $C_{60}$ on Au(100) and Au(111). From the figure it is obvious that there is no difference between the electron yields from these surfaces, even though the workfunction of Au(100) and Au(111) differs slightly [94–99].

The increase in electron yield as a function of the number of layers of $C_{60}$ may have different reasons. First of all, the SDOS is changed from a metal one to an insulator one. The band gap associated with an insulator may block or strongly restrict resonant ionization which is competitive to the Auger decay

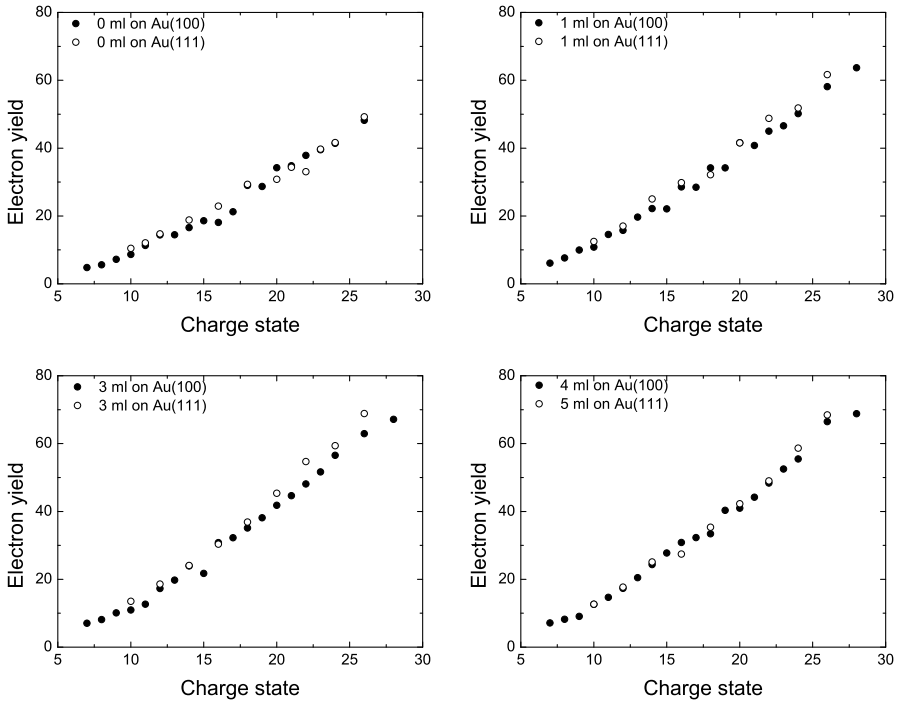


Figure 5.26: Electron yield from Au(111) and Au(100) surfaces covered with $C_{60}$ monolayers. The number of monolayers deposited on the surface is indicated in the panels.

of the hollow atom. This might lead to an increase of electron emission by the hollow atom.

Figure 5.27 is adapted from Maxwell et al. [93] and shows the SDOS of clean gold, 1 monolayer of $C_{60}$ evaporated on gold and finally the SDOS of a thick film of $C_{60}$. At first sight, the SDOS near the Fermi level/workfunction does not change dramatically when 1 monolayer of $C_{60}$ is deposited. This would imply that no band gap is introduced after deposition of one single monolayer of $C_{60}$. However, it has to be realized that the spectra shown are taken with photons which have a wavelength of tens of nanometers and therefore might still interact with the substrate as well since the $C_{60}$ molecules have a diameter of 7Å only

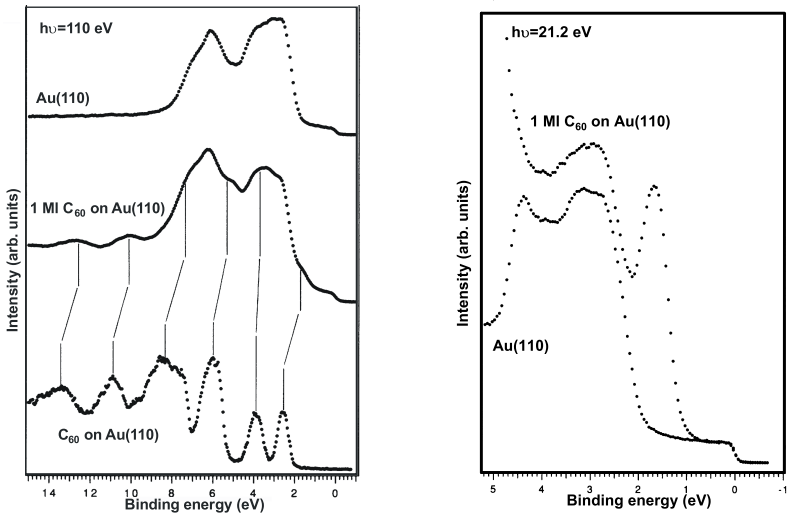


Figure 5.27: Valence photoemission spectra adapted from Maxwell et al. [93] The SDOS of the surface is altered when $C_{60}$ is evaporated on Au. Clearly visible is that a band gap is introduced when a thick layer is evaporated on Au.

[100, 101].

A second explanation for the increase in the secondary electron yield can be found in the same gure: although no band gap is introduced into the SDOS, the SDOS is greatly enhanced between 1 and 2 eV below the Fermi level. This would provide electrons for electron capture by the ion, leading to an increase in electron yield.

A third explanation for the increase in secondary electron yield could be that the open structure of the $C_{60}$ molecules allows for the electrons to escape from deeper within the surface layer. This would mean that the escape depth of the electrons is larger and electrons emitted from deeper within the solid are still able to escape to the vacuum. A similar scenario has been suggested by Meissl et al. [29] in the case of bulk LiF.

## 5.4 Conclusions

It has been unambiguously shown in this chapter that the newly built setup IISIS is excellently suited to measure secondary electron yields from ions interacting with surfaces, at least for impact angles up to 60. A clear trend is visible in electron yield when measured as function of ion charge: the electron emission shows a linear increase with potential energy.

From the measurements done, it can be concluded that not all ions undergo the same scattering trajectory. When using low incidence angles up to angles of 40°, the ion trajectories can be divided in different classes of trajectories, causing different electron yields to contribute to the average electron yield.

For the very first time electron yields have been measured on thin films. When $C_{60}$ is evaporated on an Au substrate, it shows the same behavior as an insulator: the yield is increasing as a function of the thickness of $C_{60}$ monolayers. Surprisingly enough, the major increase of the electron yield has already occurred when a film thickness of one monolayer is reached. Although several possible explanations are given, no definite scenario can be given solely on the measurements done so far. In order to investigate this further, one of the very first experiments which might provide insight in this phenomenon, would be to measure the electron yield with very slow highly charged ions since these do not penetrate the surface very deeply. This might provide insight on whether a change in SDOS/workfunction and/or the introduction of a bandgap or the escape depth of electrons is governing the change in electron yield.